materials

MDPI

Article

Modeling Dynamic Recrystallization Behavior in a Novel HIPed P/M Superalloy during High-Temperature Deformation

Qiu-Mei Yang [1,2], Yong-Cheng Lin [1,2,*], Ming-Song Chen [1] and Zi-Jian Chen [1]

[1] School of Mechanical and Electrical Engineering, Central South University, Changsha 410083, China; yangqm@csu.edu.cn (Q.-M.Y.); chenms18@csu.edu.cn (M.-S.C.); zjchen@csu.edu.cn (Z.-J.C.)
[2] State Key Laboratory of High-Performance Complex Manufacturing, Changsha 410083, China
* Correspondence: yclin@csu.edu.cn

Abstract: The dynamic recrystallization (DRX) features and the evolution of the microstructure of a new hot isostatic pressed (HIPed) powder metallurgy (P/M) superalloy are investigated by hot-compression tests. The sensitivity of grain dimension and DRX behavior to deformation parameters is analyzed. The results reveal that the DRX features and grain-growth behavior are significantly affected by deformation conditions. The DRX process is promoted with a raised temperature/true strain or a reduced strain rate. However, the grains grow up rapidly at relatively high temperatures. At strain rates of o.1 s^{-1} and 1 s^{-1}, a uniform microstructure and small grains are obtained. Due to the obvious differences in the DRX rate at various temperatures, the piecewise DRX kinetics equations are proposed to predict the DRX behavior. At the same time, a mathematical model for predicting the grain dimension and the grain growth behavior is established. To further analyze the DRX behavior and the changes in grain dimension, the hot deformation process is simulated. The developed grain-growth equation as well as the piecewise DRX kinetics equations are integrated into DEFORM software. The simulated DRX features are consistent with the test results, indicating that the proposed DRX kinetics equations and the established grain-growth model can be well used for describing the microstructure evolution. So, they are very useful for the practical hot forming of P/M superalloy parts.

Keywords: P/M superalloy; microstructure evolution; grain growth; dynamic recrystallization

Citation: Yang, Q.-M.; Lin, Y.-C.; Chen, M.-S.; Chen, Z.-J. Modeling Dynamic Recrystallization Behavior in a Novel HIPed P/M Superalloy during High-Temperature Deformation. *Materials* **2022**, *15*, 4030. https://doi.org/10.3390/ma15114030

Academic Editor: Joan-Josep Suñol

Received: 16 May 2022
Accepted: 1 June 2022
Published: 6 June 2022

1. Introduction

Owing to their excellent anti-corrosion/fatigue properties and strengths, powder metallurgy (P/M) superalloys are widely applied for manufacturing the turbine disks of aero-engines [1,2]. However, due to the high content of alloying elements and the internal defects in P/M superalloys, hot forming processes, for example, hot-extrusion and forging processes, are fairly complex [3]. Furthermore, the hot-forming process is usually accompanied by complicated deformation mechanisms such as dynamic recrystallization (DRX), dynamic recovery (DRV), etc. These deformation mechanisms are greatly influenced by the forming parameters [4–6]. Therefore, to precisely tailor the microstructures and optimize the final properties of alloy parts, it is necessary to research the sensitivity of microstructures and properties to deformation parameters. Also, accurate models should be established to predict the microstructures in hot deformed alloys [7].

During hot deformation, the microstructures can be refined and the metallurgical defects can be efficiently removed. Up until now, the material flow characteristics [8,9] and microstructure evolution [10,11] of nickel-base superalloys have been widely reported. Fang et al. [12] studied the two-pass rheological characteristics and DRX behavior of the hot-extruded P/M alloy. Zhang et al. [13] revealed the interaction between the flow behavior and γ' phase of the FGH96 superalloy and optimized the hot forming parameters. Wang et al. [14] investigated the recrystallization and densification behavior of a Ni-based

superalloy in the forging process. Zhang et al. [15] discussed the role of non-uniform precipitates on local plastic deformation in hot isostatic-pressed (HIPed) FGH96 alloy. Sreenu [16] investigated the microscopic structure features in a new P/M superalloy which was processed by the HIP route. In addition, the mathematical model is a vital way to depict the relationship between deformation conditions and rheological features, as well as the microscopic structure evolution in alloys [7,17–20]. Meanwhile, accurate mathematical models are essential to analyze/forecast material deformation behavior and the evolution of the microstructure by the finite element method (FEM) [21–23]. Recently, for the deformed P/M superalloys, some accurate mathematical models were established. For example, Liu et al. [24,25] established an equation to depict the interaction between the forming conditions and the DRX grain dimension of a hot-deformed FGH96 superalloy. Zhang et al. [26] developed the strain-compensated constitutive and ANN models to forecast the rheological characteristics for a hot-extruded P/M superalloy. Tan et al. [27] revealed that the DRX nucleation behavior and the evolution of the microstructure are sensitive to the Zener–Hollomon (Z) parameter in a hot-extruded P/M superalloy.

Though the deformation mechanisms as well as the microstructure evolution of HIPed P/M superalloys have been reported, accurate models for predicting the DRX features and grain-growth behavior are still rarely reported. In this work, the hot-compression experiments of a novel HIPed P/M superalloy are conducted. Then, the flow features, DRX mechanism, and grain features of an advanced P/M superalloy are systematically investigated. The grain dimension and DRX volume fraction (X_{drx}) are quantitatively calculated. The piecewise DRX kinetics equations and grain-growth model are established to predict the DRX and grain-growth behaviors under different deformation conditions. Then, the developed models are integrated into DEFORM software. Finally, the DRX features and microstructure evolution during hot compression are simulated.

2. Material and Experiment Procedures

The elemental components (wt. %) for the novel P/M superalloy are listed in Table 1. The size of the initial powder is about 80 μm. The test material was produced through argon atomization and hot isostatic pressing at a temperature of 1150 °C and a pressure of 150 MPa for 4 h. Figure 1 displays the primary microstructure of the HIPed P/M superalloy. The equiaxed and coarse grains are observed and the mean grain dimension is about 9.5 μm. The deformed cylinder samples were obtained from the HIPed superalloy and their radius was 4 mm and their height was 12 mm. Isothermal compression experiments were executed on the Gleeble-3500D simulator. The range of deformation amount was from 20% to 60% and that of the strain rate was from 1 to 0.001 s^{-1}. The temperature was selected from 1080 to 1170 °C. Additionally, the graphite slices were employed to minimize the friction between the molds and sample.

Table 1. The chemical compositions of the novel P/M superalloy (wt. %).

Al	Ti	Nb	Co	Cr	W	Mo	Ta	Hf	Ni
2.7–3.1	3.6–3.9	1.2–1.3	18–20	11.5–13.5	4.0–4.5	3.5–4.5	0.9–1.2	0.1–0.3	Bal.

The schematic plot of hot-deformation experiments is illustrated in Figure 2. To investigate the DRX behavior and the grain dimension in the hot-compression process, electron back-scattered diffraction (EBSD, JEOL-7001F1 FE-SEM) was applied to observe the deformed microstructures. The method of preparing EBSD samples has been reported in detail in our previous study, i.e., the samples were mechanically polished and then electrolytically polished by a solution of 10 mL $HClO_4$ and 90 mL CH_3CH_2OH at a temperature of −31 to −26 °C as well as a voltage of 23 V [28]. The EBSD test was performed at an acceleration voltage of 25 kV, step size of 0.5 μm, and a scanning area of 100 μm × 100 μm. The HKL Channel 5 software was applied to deal with EBSD data. The X_{drx} and grain size were accurately calculated by MTEX5.7.0.

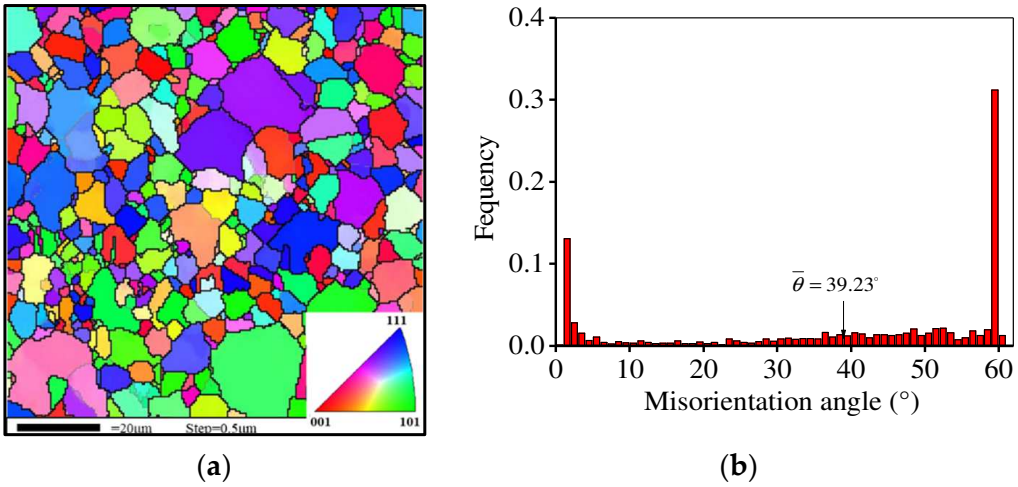

Figure 1. Initial microstructure of the HIPed superalloy: (**a**) EBSD-OIM map; (**b**) Misorientation angle distributions.

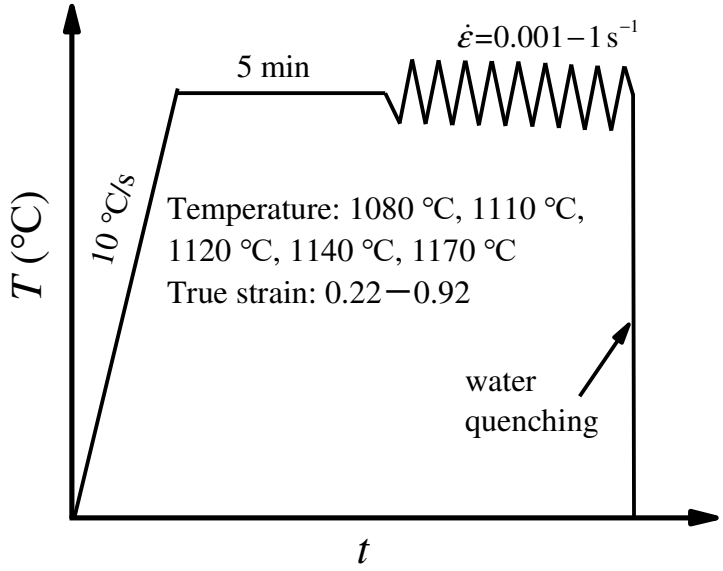

Figure 2. Schematic diagram of hot compression tests for the HIPed superalloy.

3. Results and Discussion

3.1. Rheological Characteristics and Deformation Mechanisms

Figure 3 illustrates the rheological stress of the researched superalloy under the tested conditions. The stress is large at low temperatures or high strain rates. This is because the grain boundaries (GBs) migration is weakened at low temperatures and the deformation time is short at high strain rates. In addition, the work-hardening (WH) behavior becomes obvious with a raised strain rate or a reduced temperature [29,30]. In the early period of deformation, the stress increases instantly due to the WH induced by rapid dislocation proliferation and accumulation [31,32]. As the true strain is raised, the dynamic recovery (DRV) and DRX become obvious, which results in decreased stress. As the deformation continues, stable stresses are obtained because of the kinetic equilibrium between WH, DRX, and DRV [33]. Particularly, the rheological stress exhibits a fast drop at 1120 °C/0.1 s^{-1}. This is caused by heterogeneous deformation or local deformation heating or cracking [34,35].

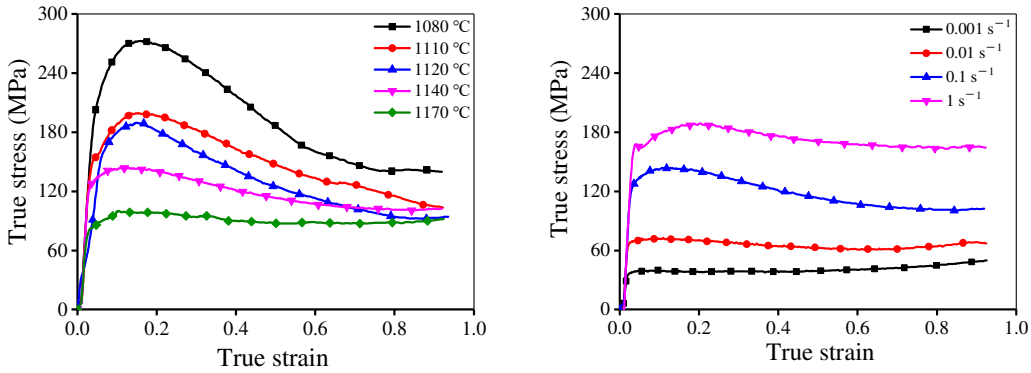

Figure 3. Typical true stress–strain curves of the HIPed superalloy at (**a**) $\dot{\varepsilon} = 0.1\ s^{-1}$; (**b**) T = 1140 °C.

3.2. The Evolution of Microstructure

3.2.1. Influence of True Strain on DRX Behavior and Grain Dimension

The grain-orientation spread (GOS) method can reflect the orientation gradient within grains and evaluate the DRX degree in the deformed alloy [36]. Here, the DRX and deformed grains are recognized by the GOS method [37]. The calculation equation is expressed as [38]:

$$\mathrm{GOS} = \frac{1}{J(a)}\sum_{b}\omega_{ab} \quad (1)$$

where $J(a)$ shows the pixels amount in grain a and ω_{ab} shows the misorientation degree between the orientation of pixel position b and average orientation of grain a. According to the GOS distribution of the complete DRX sample and GOS division principle [39], the grains with GOS $< 3°$ are defined as DRX grains.

When the temperature and strain rate are 1110 °C and 0.1 s^{-1}, respectively, the GOS distribution at the true strain of 0.22, 0.51, and 0.92 is demonstrated in Figure 4. Obviously, there are some changes in DRX behavior and grain dimension at different strains. As the true strain is raised, the mean GOS and average kernel misorientation (KAM) decreases but the X_{drx} increases. Meanwhile, the average grain dimension is reduced from 7.18 to 4.21 μm when the strain increases from 0.22 to 0.92, whereas the mean DRX grain dimension (d_{drx}) increases. At 0.22 (Figure 4a), a mass of substructures and serrated GBs appear. Meanwhile, fine DRX grains and necklace structures are observed at the serrated/bulging GBs because the serrated GBs have a high local orientation or strain gradient for DRX nucleation. Obviously, discontinuous dynamic recrystallization (DDRX) occurs [40,41]. At 0.22, the GOS (7.04°)/KAM (1.88°) values are relatively high and the X_{drx} (15.56%) is low. However, the average grain size is large, which is attributable to the high dislocation density and the low-deformation storage energy. The original GBs are gradually covered by DRX grains and the mean GOS and KAM rapidly decrease when the true strain is 0.51. In addition, the X_{drx} increases significantly. Although the DRX grains grow up, the average grain size decreases to 4.39 μm because of the annihilation/rearrangement of dislocations and the migration of GBs [42–44]. When the true strain is further raised to 0.92 (Figure 4c), the number of grains with high GOS values further decreases and the KAM also declines to 0.56°. In addition, the DRX degree increases. As the DRX grains further grow up, a uniform microstructure is obtained.

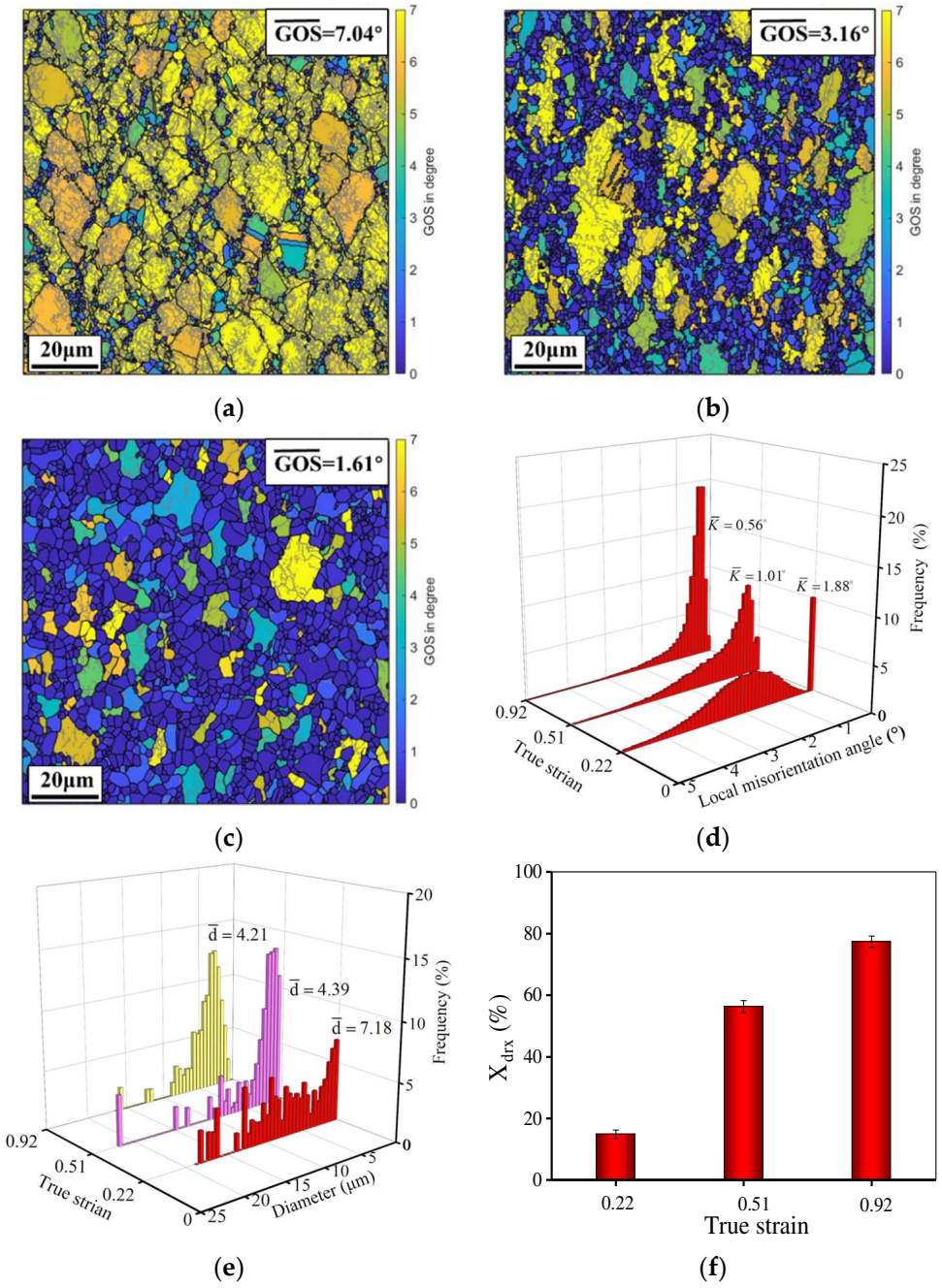

Figure 4. GOS maps of the HIPed superalloy deformed at the true strain of (**a**) 0.22; (**b**) 0.51; (**c**) 0.92 [28]; (**d**) the local misorientation angle; (**e**) average grain size distribution; (**f**) area fraction of DRX (HAGBs and LAGBs correspond to the black line and gray line, respectively. The temperature and strain rate are 1110 °C and 0.1 s^{-1}, respectively).

3.2.2. Influence of Strain Rate on the DRX Behavior and Grain Dimension

Figure 5 displays the evolution of DRX behavior and grain dimension at diverse strain rates. Here, the true strain is 0.92 and the temperature is 1140 °C. Some serrated GBs and tiny DRX grains can be found, which reveals the occurrence of DDRX [34]. As the strain rate increases from 0.001 s^{-1} to 0.1 s^{-1}, the average KAM and GOS increase but the X_{drx} decreases. Meanwhile, tiny DRX grains are found and the mean grain dimension decreases because the large strain rate can produce high strain energy and accelerate the development of substructures with a mass of dislocations. It is conducive to DRX nucleation [45]. In addition, previous reports show that less time for deformation and γ' phase pinning results

in a low X_{drx} and fine grains at a high strain rate [46]. The grains with high GOS have hardly been observed at 1140 °C and the X_{drx} at three strain rates are higher than 95%, which indicates the DRX is complete.

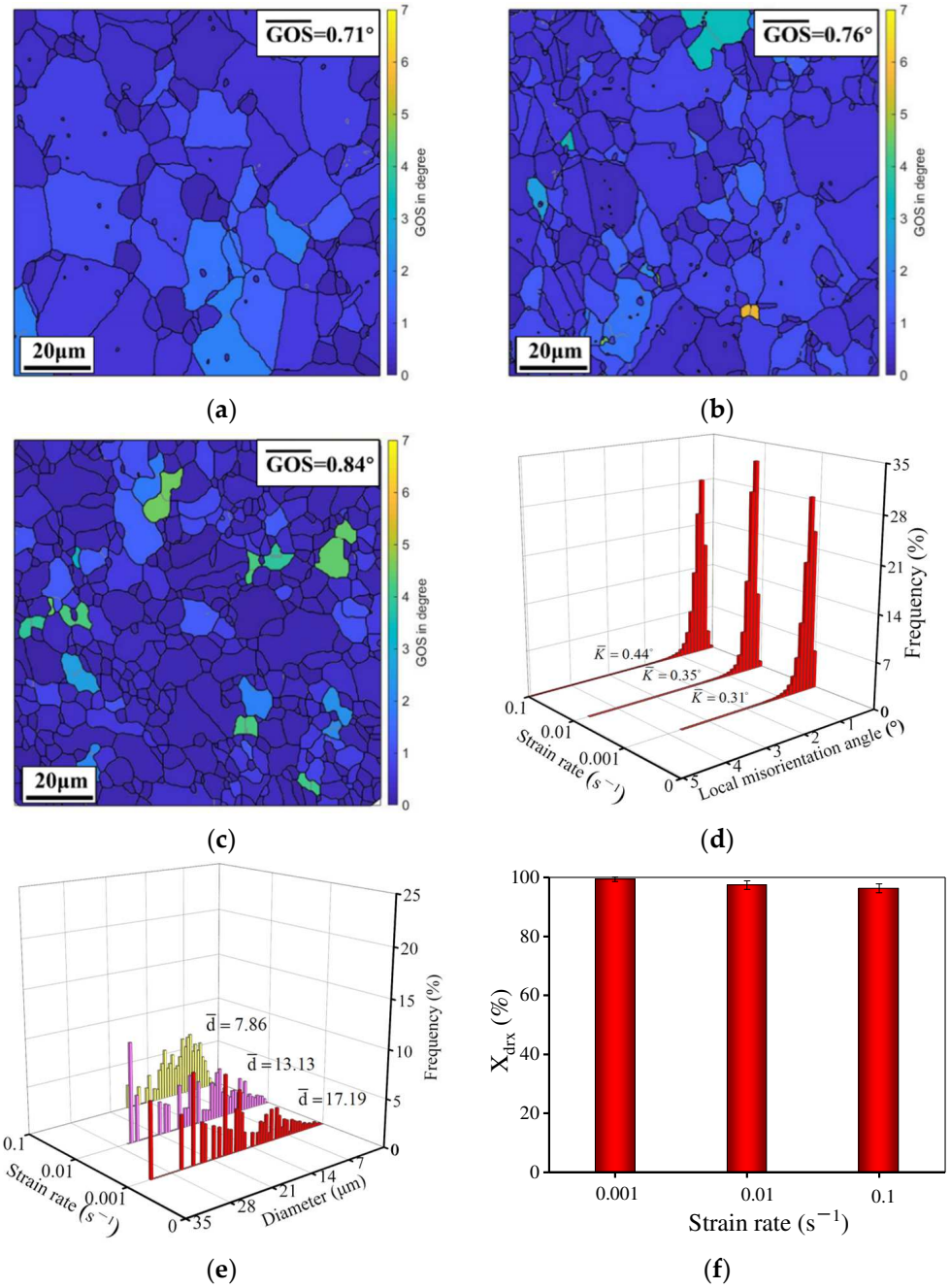

Figure 5. GOS maps of the HIPed superalloy deformed at a strain rate of (**a**) 0.001 s^{-1}; (**b**) 0.01 s^{-1}; (**c**) 0.1 s^{-1} [28]; (**d**) local misorientation angle; (**e**) average grain size distribution; (**f**) area fraction of DRX (the temperature and true strain are 1140 °C and 0.92, respectively).

3.2.3. Influence of Temperature on the DRX Behavior and Grain Dimension

When the true strain is 0.92 and the strain rate is 0.1 s^{-1}, the relationship between temperature and GOS is depicted in Figure 6. The mean value of GOS declines but the average grain size and X_{drx} increase when the temperature is raised. At low temperatures (Figure 6a,b), the grains with high GOS and fine DRX grains are observed and the KAM is high (0.87° and 0.71°). It indicates the high dislocation density in grains and the limited DRX. When the temperature is raised to 1140/1170 °C (Figure 6c,d), the enhanced DRX

induces a decrease in the mean GOS and KAM. Also, the X_{drx} increases significantly (Figure 6f). This is attributed to the high temperature enhancing the movement of GBs and the mobility/diffusion of dislocations. In addition, the mean grain size increases to 13.48 μm due to the rapid growth of DRX grains. The γ′ phase is sufficiently dissolved, which weakens the pinning effect on GBs [47]. Particularly, the DRX rate is significantly disparate at diverse temperatures. In Figure 6h, when the temperature is below 1120 °C, the X_{drx} is lower than 82%. However, the DRX is almost complete at 1140 °C.

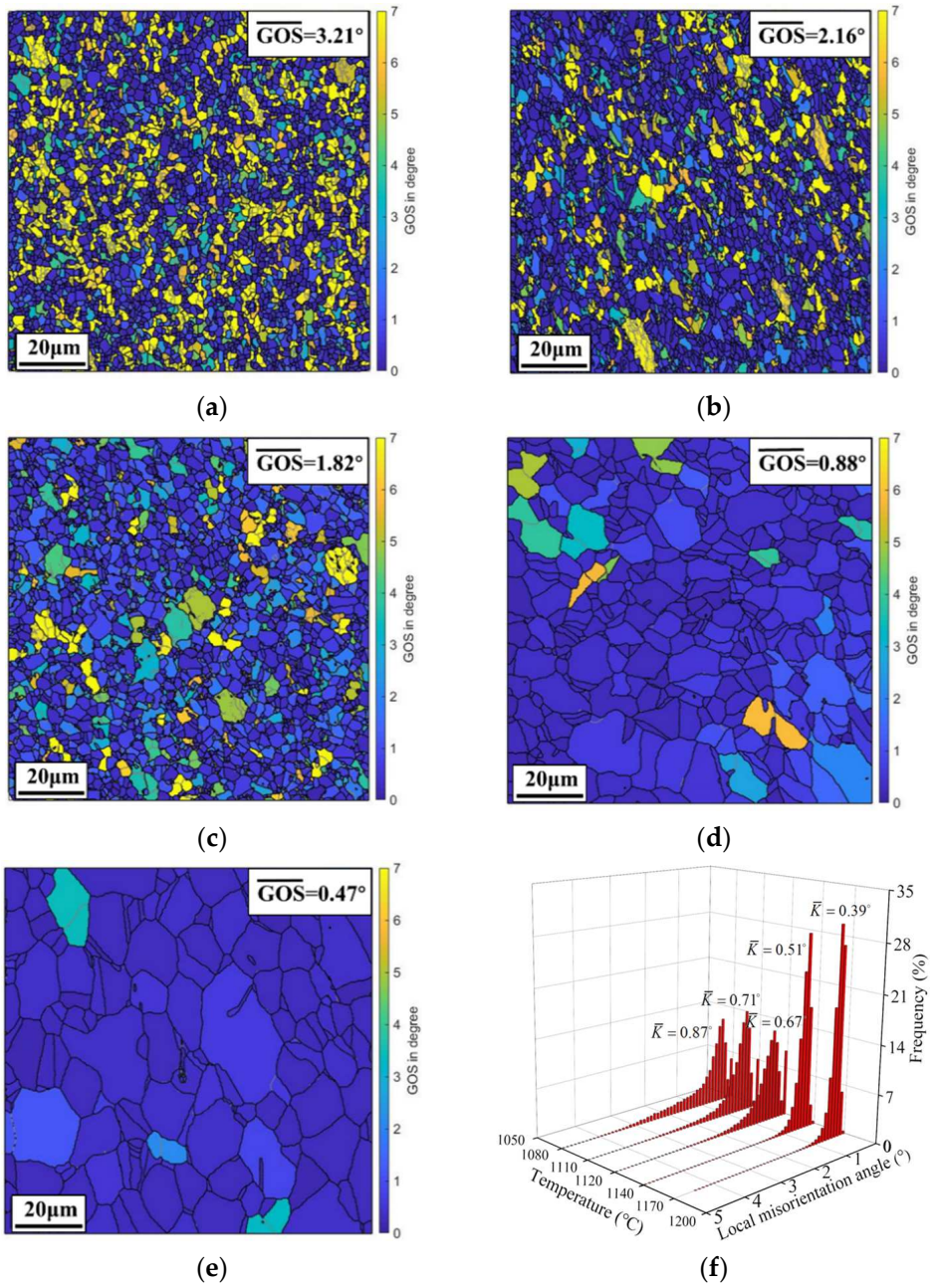

Figure 6. *Cont.*

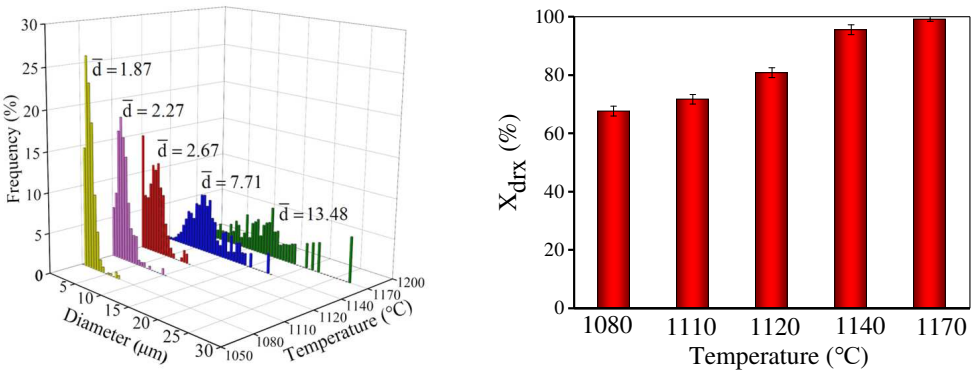

Figure 6. GOS maps of the HIPed superalloy deformed at temperatures of (**a**) 1080 °C; (**b**) 1110 °C [28]; (**c**) 1120 °C; (**d**) 1140 °C; (**e**) 1170 °C; (**f**) the local misorientation angle; (**g**) average grain size distribution; (**h**) area fraction of DRX (the strain rate is 1 s^{-1} and true strain is 0.92).

Summarily, the DRX behavior and grain features of the studied HIPed P/M superalloy are dramatically affected by the deformation amount, temperature, and strain rate. Hence, the contour maps to depict the effects of deformation conditions on DRX volume fraction and average DRX grain size are demonstrated in Figure 7. Obviously, the DRX is enhanced with the raised temperature or the reduced strain rate. The colors and values of the contour maps are very different in terms of the raised temperature when the strain rate is constant. When the temperature is below 1120 °C, a weak DRX is observed. However, a full DRX can be achieved at 1140/1170 °C. Also, the DRX rates are different at various temperatures. This is because the movement of GBs is enhanced by the time and energy at high temperatures. Therefore, based on the effects of temperature on DRX mechanisms, the piecewise DRX kinetics models are proposed in Section 3.3.

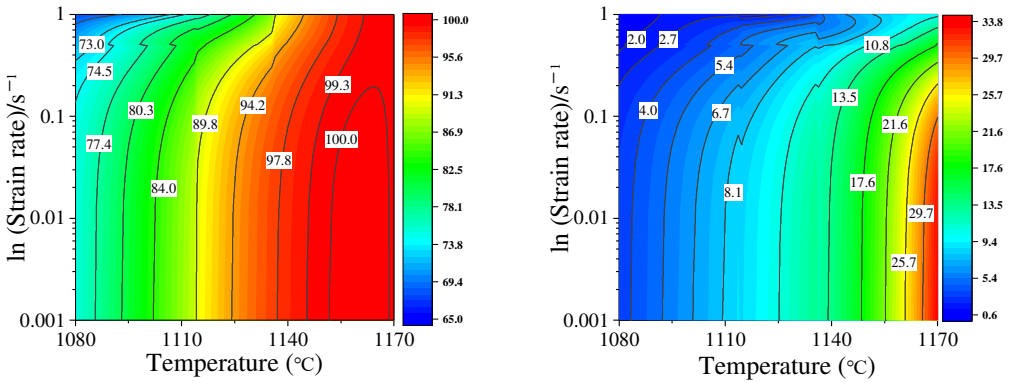

Figure 7. Contour maps at different deformation conditions: (**a**) DRX volume fraction; (**b**) average DRX grain size.

3.3. DRX Kinetics Model

Generally, the critical strain (ε_c) corresponding to DRX is decided by $\theta - \sigma$ curves [34,48]. Here, $\theta = \frac{d\sigma}{d\varepsilon}$ shows the WH rate, σ represents the true stress, and ε is the true strain. According to Poliak's study [38], the ε_c for DRX is equal to the minimum spot on the $\theta - \sigma$ curve and θ is expressed as a third-order polynomial function:

$$\theta = A_1\sigma^3 + A_2\sigma^2 + A_3\sigma + A_4 \quad (2)$$

where A_1, A_2, A_3, and A_4 represent material constants.

Then, Equation (2) is also expressed as:

$$\frac{d^2\theta}{d\sigma^2} = 6A_1\sigma + 2A_2 \quad (3)$$

For $\frac{d^2\theta}{d\sigma^2} = 0$, the critical stress ($\sigma_c$) can be expressed as:

$$\sigma_c = -A_2/3A_1 \quad (4)$$

Based on the measured rheological stresses, the σ_c and ε_c can be determined. Figure 8 displays the values of under various conditions. Obviously, the reduced temperature or the raised strain rate increase ε_c.

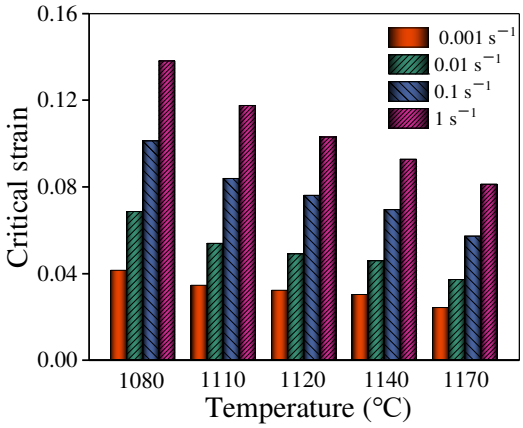

Figure 8. The column bars of ε_c at different temperatures and strain rates.

Generally, ε_c can be evaluated by:

$$\varepsilon_c = a_1\dot{\varepsilon}^{l_1}\exp\left(\frac{Q_1}{RT}\right) \quad (5)$$

where R is the constant for gas (8.314 J/(K·mol)). In addition, a_1 and Q_1 are material parameters, which can be decided by least square linear fitting of $\ln\varepsilon_c$–10,000/T and $\ln\varepsilon_c - \ln\dot{\varepsilon}$ plots, respectively, as displayed in Figure 9. Thus, ε_c is determined as:

$$\varepsilon_c = 1.794\times10^{-5}\dot{\varepsilon}^{0.1731}\exp\left(\frac{101,090.13}{RT}\right) \quad (6)$$

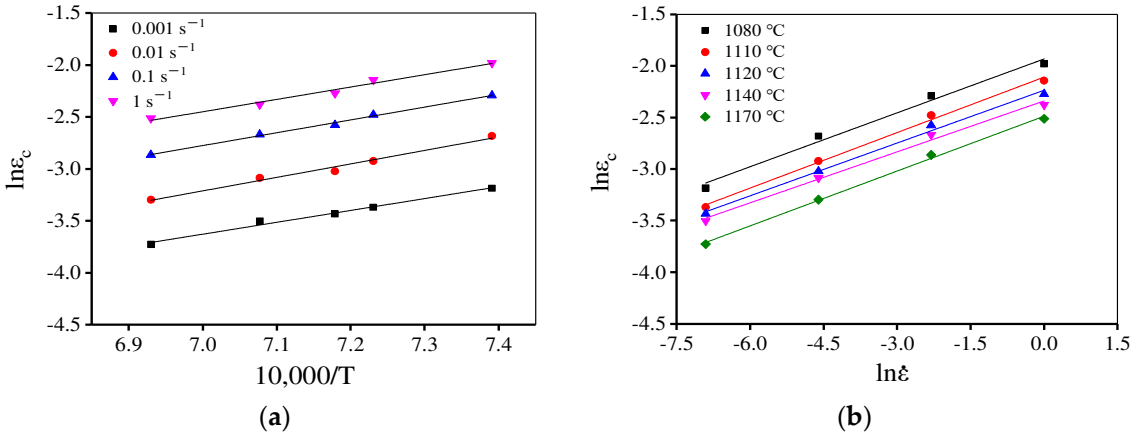

Figure 9. The relationship between (**a**) $\ln\varepsilon_c$–10,000/T and (**b**) $\ln\varepsilon_{0.5} - \ln\dot{\varepsilon}$.

Figure 10 displays the variations of X_{drx} with the true strain at 1140 °C/0.001 s^{-1}. The value of X_{drx} is small in the initial incubation stage. After this incubation period, the DRX is accelerated and finally tends to be stable. The $\varepsilon_{0.5}$ can be obtained through the $X_{drx} - \varepsilon$ curve (Figure 10a). Figure 10b illustrates the value of $\varepsilon_{0.5}$ at various compression conditions. The reduced strain rate or the raised temperature can decrease $\varepsilon_{0.5}$. Similarly, $\varepsilon_{0.5}$ is related to deformation parameters [49], i.e.,

$$\varepsilon_{0.5} = a_2 \dot{\varepsilon}^{l_2} \exp\left(\frac{Q_2}{RT}\right) \quad (7)$$

where a_2, l_2, and Q_2 represent material parameters, which can be evaluated by $\ln \varepsilon_{0.5}$–10,000/T and $\ln \varepsilon_{0.5} - \ln \dot{\varepsilon}$ plots, respectively, as illustrated in Figure 11. Hence, $\varepsilon_{0.5}$ is determined as:

$$\varepsilon_{0.5} = 4.577 \times 10^{-7} \dot{\varepsilon}^{0.114} \exp\left(\frac{159,420.7}{RT}\right) \quad (8)$$

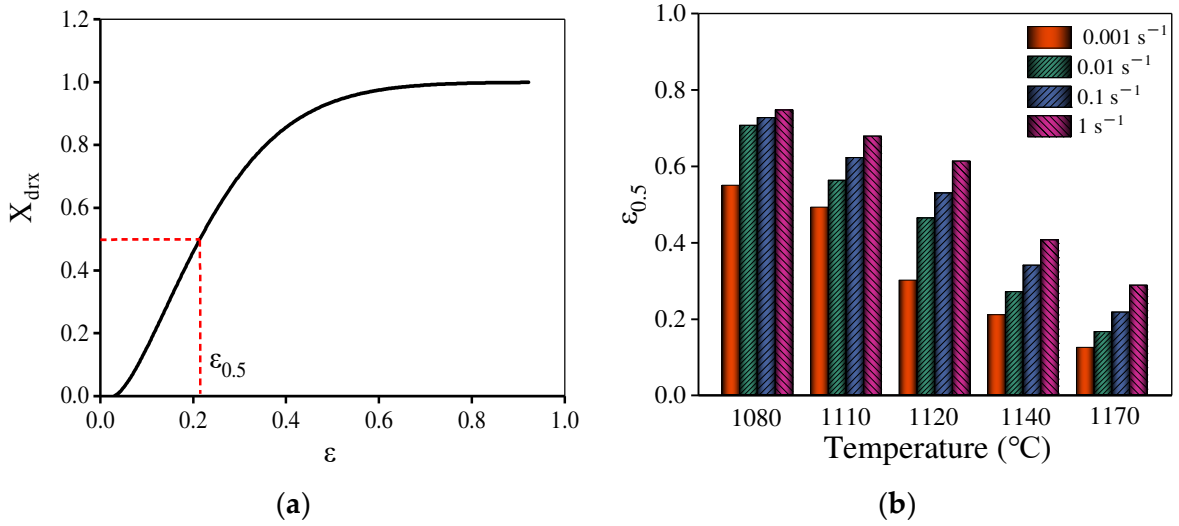

Figure 10. (**a**) Relationship between X_{drx} and ε at 1140 °C/0.001 s^{-1}. (**b**) $\varepsilon_{0.5}$ at different deformation conditions.

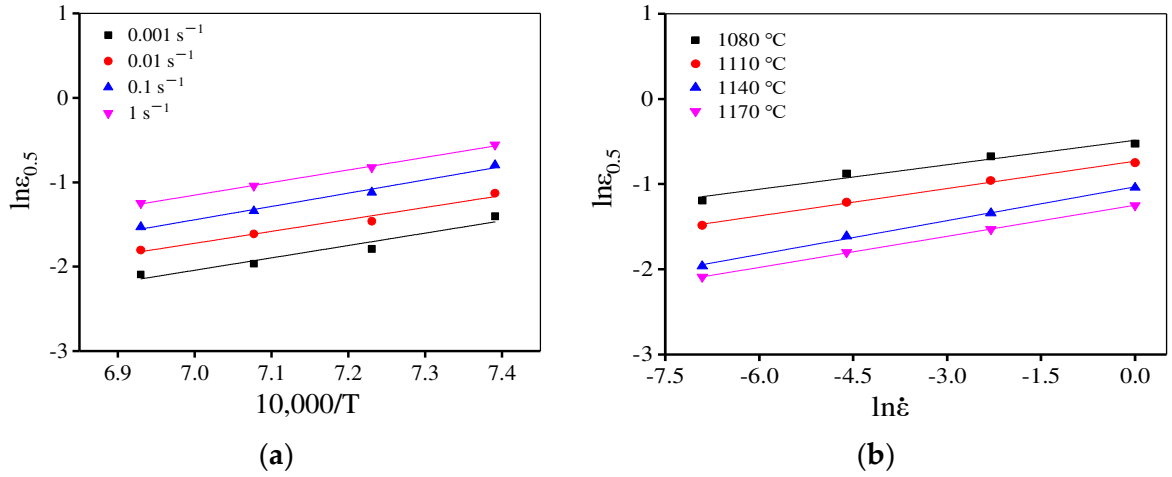

Figure 11. Relationship between $\varepsilon_{0.5}$ and deformation parameters (**a**) $\ln \varepsilon_{0.5}$ –10,000/T and (**b**) $\ln \varepsilon_{0.5} - \ln \dot{\varepsilon}$.

In Figure 10, the variations in X_{drx} with the strain are similar to a sigmoidal curve, which can be described as [32]:

$$X_{drx} = 1 - \exp\left[-0.693\left(\frac{\varepsilon - \varepsilon_c}{\varepsilon_{0.5} - \varepsilon_c}\right)^n\right] \qquad (\varepsilon > \varepsilon_c) \tag{9}$$

where n is a material constant. X_{drx}, ε, ε_c, and $\varepsilon_{0.5}$ separately represent the DRX volume fraction, true strain, critical strain, and the strain where X_{drx} reaches 50%. Figure 12 displays $\ln(-\ln(1 - X_{drx})) - \ln((\varepsilon - \varepsilon_c)/(\varepsilon_{0.5} - \varepsilon_c))$ plot, and the n is determined through the linear fitting of this plot. Then, the DRX kinetics models are determined as:

$$\begin{cases} X_{drx} = 1 - \exp\left[-0.693\left(\frac{\varepsilon - \varepsilon_c}{\varepsilon_{0.5} - \varepsilon_c}\right)^{2.15}\right] \\ \varepsilon_c = 1.747 \times 10^{-5} \dot{\varepsilon}^{0.1737} \exp\left(\frac{101{,}502.36}{RT}\right) \\ \varepsilon_{0.5} = 4.577 \times 10^{-7} \dot{\varepsilon}^{0.114} \exp\left(\frac{159{,}420.7}{RT}\right) \end{cases} \tag{10}$$

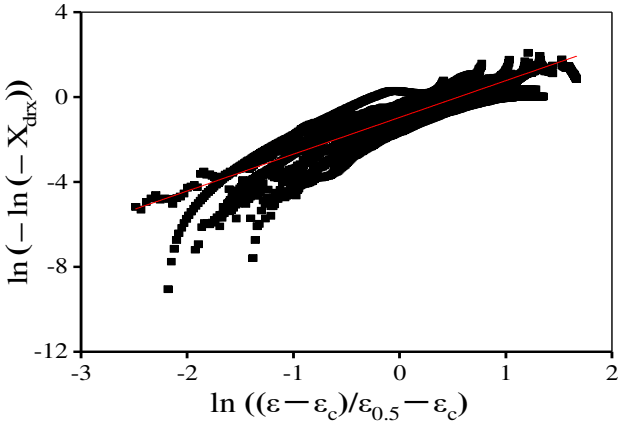

Figure 12. The relationship between $\ln(-\ln(1 - X_{drx}))$ and $\ln((\varepsilon - \varepsilon_c)/(\varepsilon_{0.5} - \varepsilon_c))$.

Figure 13 gives the relationship between the strain rate/ε and the calculated X_{drx}. Also, the comparisons between the calculated and experimental X_{drx} are represented. To validate the precision of traditional DRX kinetics equations, the average absolute relative error (AARE) and correlation coefficient € are calculated, i.e.,

$$\mathrm{R} = \frac{\sum_{i=1}^{N}(E_i - \overline{E})(P_i - \overline{P})}{\sqrt{\sum_{i=1}^{N}(E_i - \overline{E})^2 (P_i - \overline{P})^2}} \tag{11}$$

$$AARE = \frac{1}{N}\sum_{i=1}^{N}\left|\frac{E_i - P_i}{E_i}\right| \times 100 \tag{12}$$

where E_i is the measured value and P_i shows the calculated one. Meanwhile, the measured mean value is expressed as E and the calculated mean value is defined as P. In Figure 13, the traditional DRX equation can well describe the DRX behavior at high temperatures (1140–1170 °C). However, when the forming temperatures are below 1110 °C, the predicted X_{drx} is much higher than the experimental value and the R between experimental and predicted X_{drx} is only 0.15. Meanwhile, the predicted $\varepsilon_{0.5}$ value is low, which indicates that DRX occurs in advance. According to the above EBSD observations, due to a large number of dissolved γ' phases [50] and enough energy for GBs' migration at high temperatures, DRX occurs rapidly. However, the γ' phase is difficult to dissolve and the deformation time is short with the raised strain rate and the reduced temperature, resulting in the decreased DRX rate. Thus, the DRX rates are quite different at various deformation temperatures. So,

the traditional kinetics model cannot accurately predict the DRX behavior under different deformation conditions.

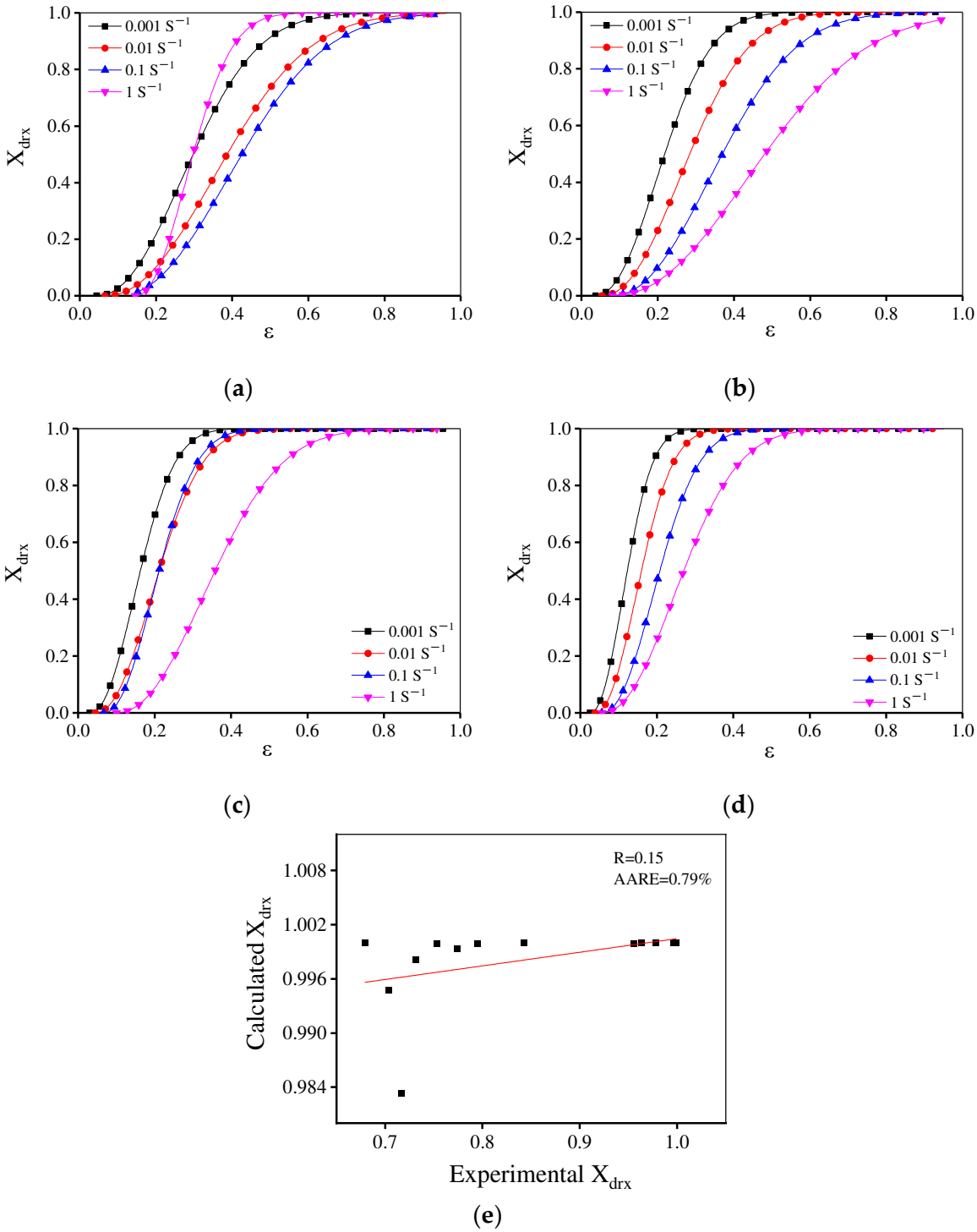

Figure 13. The effects of strain rate and strain on X_{drx} at (**a**) 1080 °C; (**b**) 1110 °C; (**c**) 1140 °C; (**d**) 1170 °C. (**e**) The comparisons between the calculated and experimental X_{drx}.

In Figure 10b, when the temperature is below 1120 °C $\varepsilon_{0.5}$ is high. However, at 1140 °C and 1170 °C, $\varepsilon_{0.5}$ is low indicating that the DRX rate is significantly different at various temperatures. Combined with the microstructure evolution discussed in Section 3.2.3, to precisely describe the DRX behavior for the present alloy, the piecewise equations can be used to predict $\varepsilon_{0.5}$ and the segmented temperature is 1200 °C. The material parameters

are determined by least square linear fitting of $\ln \varepsilon_{0.5}$–10,000/T and $\ln \varepsilon_{0.5} - \ln \dot{\varepsilon}$ plots, as shown in Figures 14 and 15. Then, $\varepsilon_{0.5}$ is determined as:

$$\varepsilon_{0.5} = 3.05 \times 10^{-5} \dot{\varepsilon}^{0.059} \exp\left(\frac{114,876.8}{RT}\right) \qquad (T = 1080 - 1120\ ^{\circ}\mathrm{C}) \tag{13}$$

$$\varepsilon_{0.5} = 5.67 \times 10^{-12} \dot{\varepsilon}^{0.107} \exp\left(\frac{294,773.5}{RT}\right) \qquad (T = 1120 - 1170\ ^{\circ}\mathrm{C}) \tag{14}$$

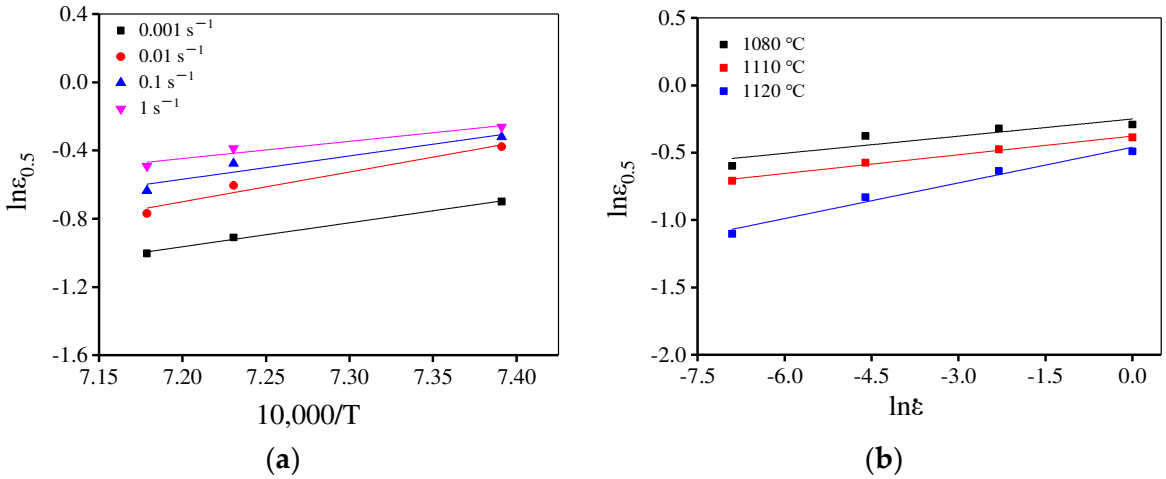

Figure 14. Relationship between $\varepsilon_{0.5}$ and deformation conditions (**a**) $\ln \varepsilon_{0.5}$ –10,000/T and (**b**) $\ln \varepsilon_{0.5} - \ln \dot{\varepsilon}$.

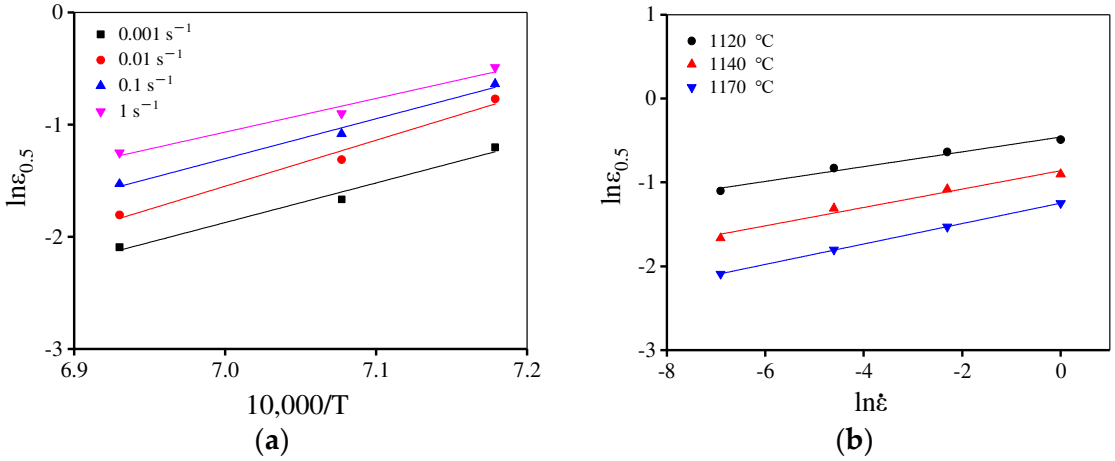

Figure 15. Relationship between $\varepsilon_{0.5}$ and deformation parameters (**a**) $\ln \varepsilon_{0.5}$ –10,000/T and (**b**) $\ln \varepsilon_{0.5} - \ln \dot{\varepsilon}$.

In Figure 16, the values of material constant n are determined in the range of 1080–1120 °C and 1120–1170 °C, respectively. Consequently, the proposed piecewise DRX kinetics equations are determined as:

$$\begin{cases} X_{\mathrm{drx}} = 1 - \exp[-0.693(\frac{\varepsilon - \varepsilon_c}{\varepsilon_{0.5} - \varepsilon_c})^n] \\ n = \begin{cases} 1.61 & (T = 1080 - 1120\ ^{\circ}\mathrm{C}) \\ 1.48 & (T = 1120 - 1170\ ^{\circ}\mathrm{C}) \end{cases} \\ \varepsilon_c = 1.79 \times 10^{-5} \dot{\varepsilon}^{0.173} \exp(\frac{101,090.1}{RT}) \\ \varepsilon_{0.5} = \begin{cases} 3.05 \times 10^{-5} \dot{\varepsilon}^{0.059} \exp(\frac{114,876.8}{RT}) & (T = 1080 - 1120\ ^{\circ}\mathrm{C}) \\ 5.67 \times 10^{-12} \dot{\varepsilon}^{0.107} \exp(\frac{294,773.5}{RT}) & (T = 1120 - 1170\ ^{\circ}\mathrm{C}) \end{cases} \end{cases} \tag{15}$$

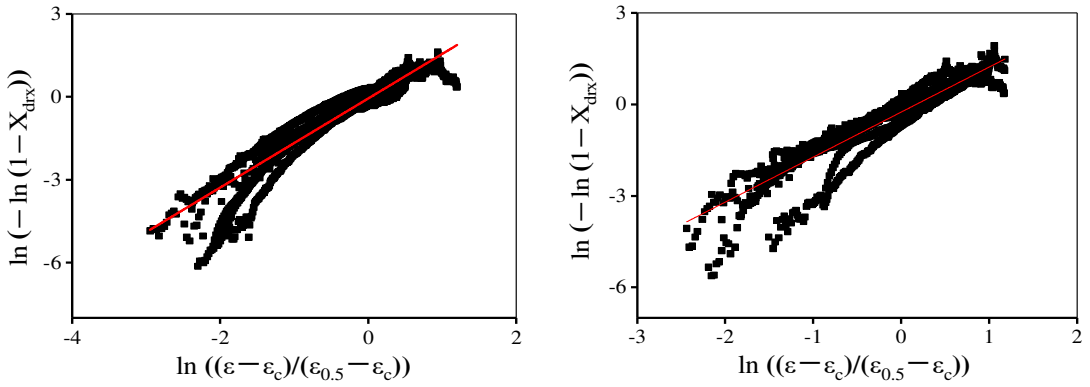

Figure 16. The relationship between $\ln(-\ln(1-X_{drx}))$ and $\ln((\varepsilon-\varepsilon_c)/(\varepsilon_{0.5}-\varepsilon_c))$ at (**a**) 1080–1120 °C and (**b**) 1120–1170 °C.

Figure 17 gives the variations in the calculated X_{drx} with the strain. Also, the comparisons between the calculated and experimental X_{drx} are represented. The calculated values are very close to the experimental ones. To confirm the precision of the proposed piecewise DRX kinetics equations, R and AARE are calculated. The AARE value is 2.3% and the R value is 0.992. Hence, the DRX behavior of the present HIPed P/M superalloy during hot compression can be accurately described by the proposed piecewise DRX kinetics equations.

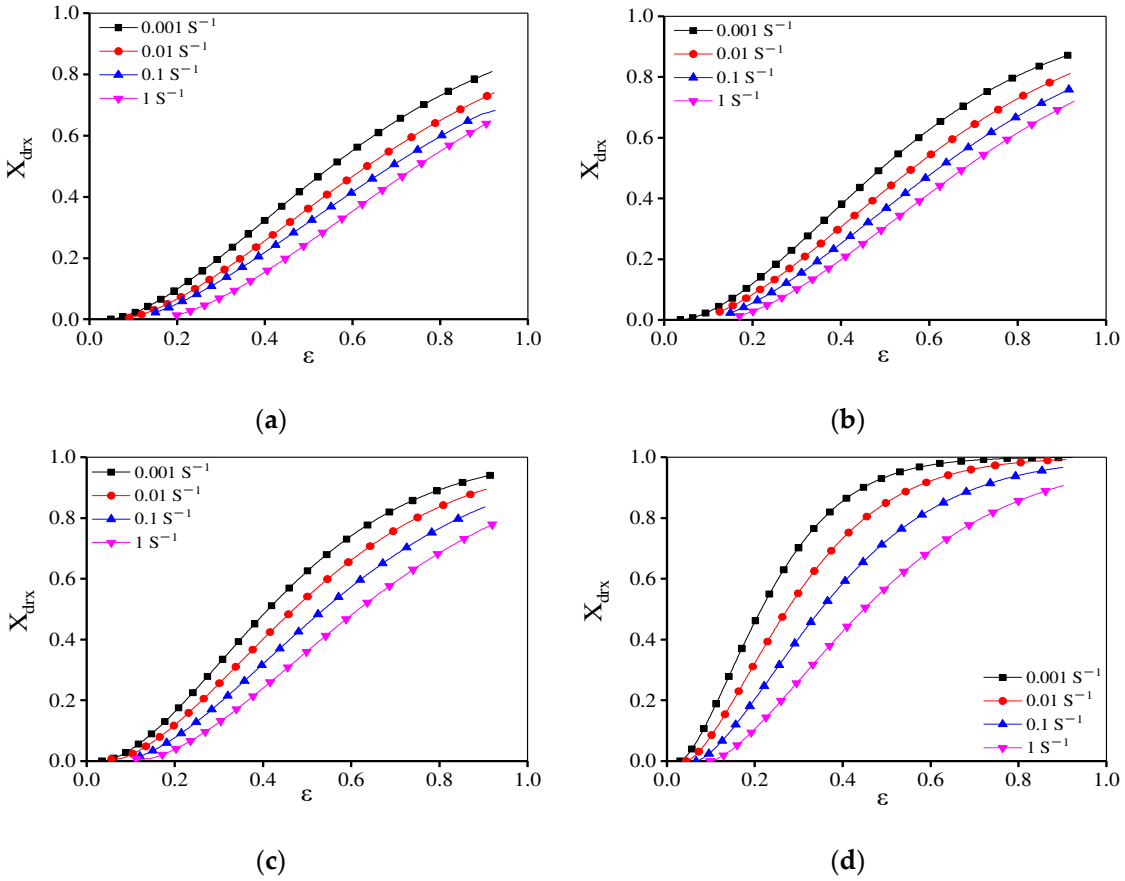

Figure 17. *Cont.*

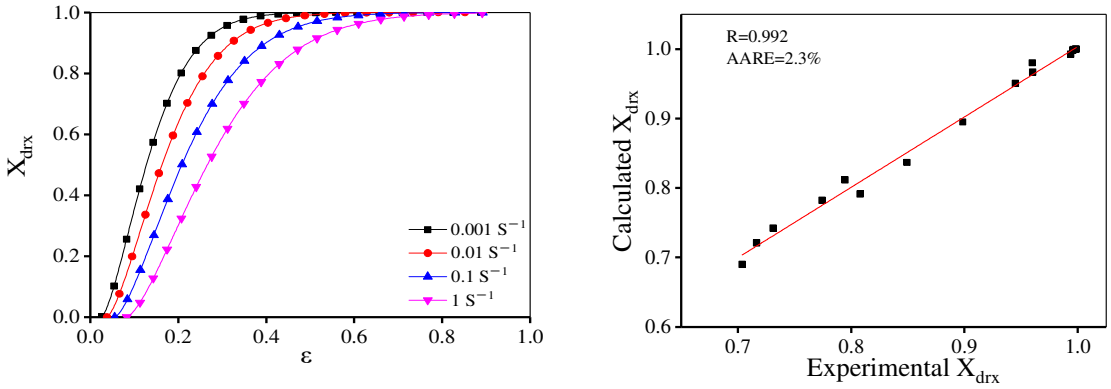

(**e**) (**f**)

Figure 17. The effects of strain rate and strain on X_{drx} at (**a**) 1080 °C; (**b**) 1110 °C; (**c**) 1120 °C; (**d**) 1140 °C; and (**e**) 1170 °C. (**f**) The comparisons between the calculated and experimental X_{drx}.

The DRX grain size (d_{drx}) in the stable deformation stage is listed in Table 2. Obviously, the reduced strain rate or the raised temperature can increase d_{drx}. Generally, d_{drx} is connected with the compression parameters, which is evaluated through Sellars's empirical equation [32,51]. Hence, according to experimental data, d_{drx} is determined as:

$$d_{drx} = 1.76 \times 10^{15} \dot{\varepsilon}^{-0.16} \exp\left(\frac{-393,644.47}{RT}\right) \quad (16)$$

Table 2. The size of DRX grain (d_{drx}) at the steady-state deformation stage (μm).

Temperature/Strain Rate	0.001 s^{-1}	0.01 s^{-1}	0.1 s^{-1}	1 s^{-1}
1080 °C	3.53	2.23	1.64	1.36
1110 °C	6.98	4.37	3.24	2.32
1140 °C	17.07	12.46	7.52	7.36
1170 °C	33.75	21.73	14.73	10.29

Figure 18 demonstrates the comparisons between the calculated/experimental d_{drx}. The calculated AARE value is 2.5% and the R is 0.991. Meanwhile, the mean grain dimension is demonstrated as:

$$d_i = d_{drx}X + d_0(1 - X) \quad (17)$$

where d_{drx} represents the size of DRX grain, d_0 shows the initial grain size, and X represents the DRX volume fraction. Similarly, d_{drx} is demonstrated as:

$$d_{drx} = 1.76 \times 10^{15} \dot{\varepsilon}^{-0.16} \exp\left(\frac{-393,644.47}{RT}\right) \quad (18)$$

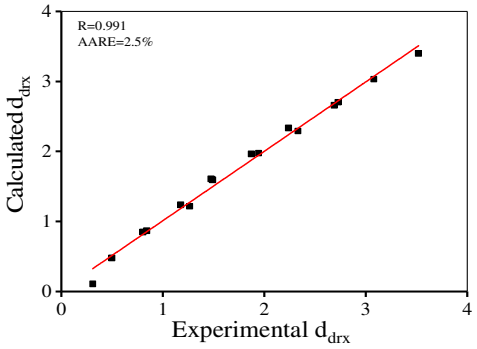

Figure 18. Comparisons between the calculated and experimental d_{drx}.

3.4. Finite-Element Simulation of DRX Behavior and Grain-Dimension Evolution

In order to simulate DRX behavior and grain-dimension evolution in this HIPed superalloy during hot compression, the proposed piecewise DRX kinetics equations and grain-growth model are integrated into the DEFORM software through the development of the subprogram. The program flowchart to simulate the DRX behavior and grain size is illustrated in Figure 19. First of all, the hot-compression parameters and the initial microstructure are inputted. Then, for a given time increment, ε_c is calculated. If $\varepsilon < \varepsilon_c$, the present operation is continued. At the same time, the current strain rate state ($\dot{\varepsilon}$) is evaluated. If $\varepsilon > \varepsilon_c$ and $\dot{\varepsilon}(t) > 0$, DRX will occur and the X_{drx}/grain-size dimension will be counted. If $X_{\mathrm{drx}} > 95\%$, full DRX is finished. Meanwhile, the current grain dimension is regarded as the mean DRX grain dimension. If $X_{\mathrm{drx}} < 95\%$, the mean grain dimension is calculated according to the grain-growth model. Finally, when the deformation is finished, the X_{drx} and grain size are outputted. Figure 20 displays the hot-deformed finite-element geometric model, which is composed of a billet and upper and lower dies. The three-dimensional (3D) transmutable type is applied to the hot-compressed block, whereas the 3D-resolution rigid body is used as a mold. During hot compression, the P/M superalloy workpiece and dies are regarded as the variable object and immutable objects, respectively. The radius of the workpiece is Φ 4 mm and the height is 12 mm. The simulated parameters are the same as those of the present experiments. The moving velocity of the top die is converted from the experimental strain rate. The shear friction is selected and the friction factor is 0.12. The element number of the billet and dies are 30,000 and 8000, respectively.

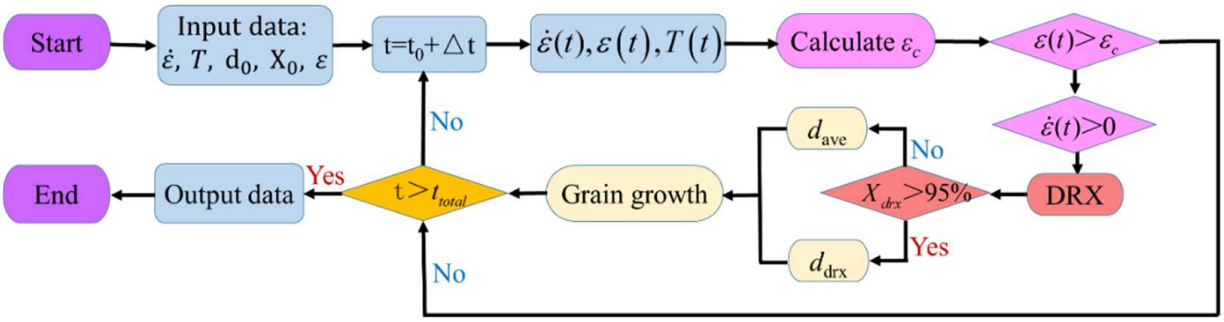

Figure 19. Flow chart to simulate the DRX behavior and grain size.

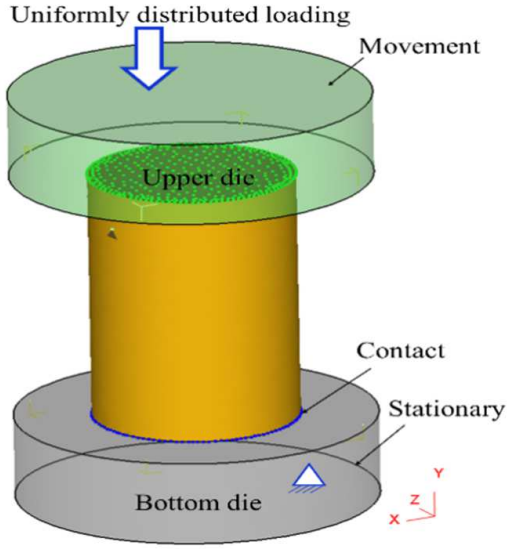

Figure 20. The FEM model for hot compression.

The evolution of the equivalent strain at diverse deformation parameters is demonstrated in Figure 21. The distribution of equivalent strain almost changes symmetrically along the compression axis and radial direction. Three typical deformation regions (large, free, and difficult deformation) are observed. The center is a high-strain area, namely the large deformation zone resulting from the triaxial constringent stress and small frictional force, whereas the end faces that have contact with the dies are low-strain areas, i.e., the difficult deformation regions. Compared with the equivalent strain in the central region, the equivalent strain at the edge and end of the expansion site is smaller. In addition, the uniformity of the strain distribution in the central region is improved with a reduced strain rate or a raised temperature.

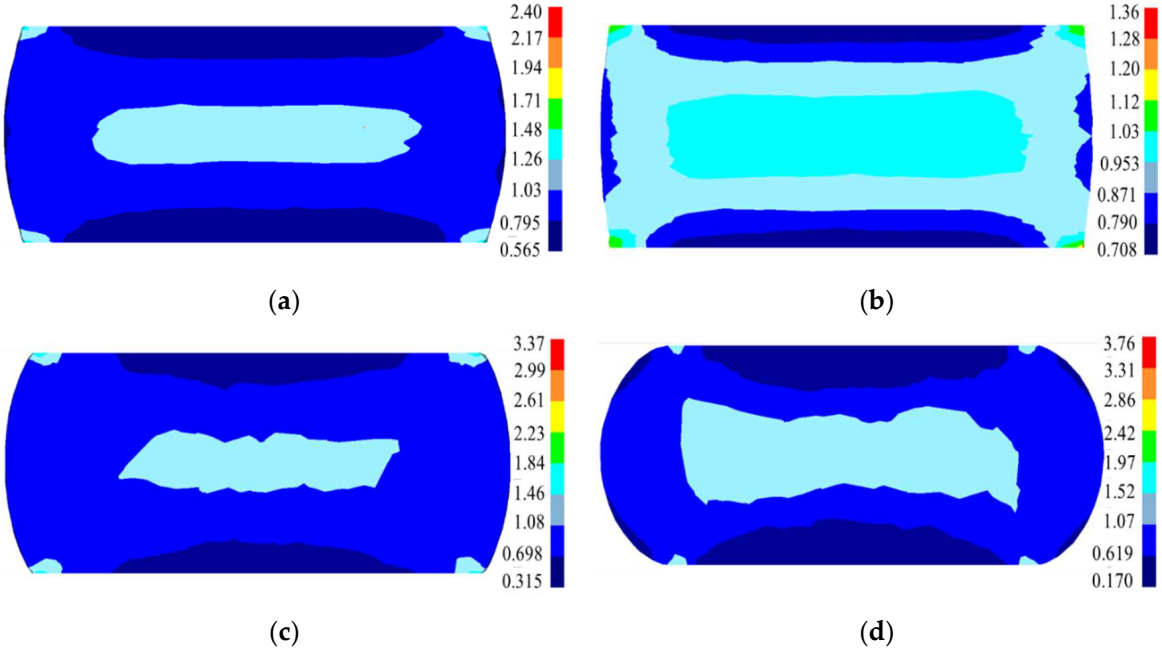

Figure 21. The equivalent plastic strain at (**a**) 1110 °C/0.1 s^{-1}; (**b**) 1140 °C/0.1 s^{-1}; (**c**) 1110 °C/0.01 s^{-1}; and (**d**) 1110 °C/1 s^{-1}.

The distribution of the predicted X_{drx} at diverse deformation parameters is displayed in Figure 22. There are obvious differences in the DRX degree in the different regions, which is due to the non-uniformity deformation caused by the friction between the dies and billet. The DRX degree is the highest in the large deformation zone, whereas the lowest is in the difficult deformation region. The simulated X_{drx} in the large deformation zone increases with a reduced strain rate or a raised temperature. They are 80%, 97%, 85.9%, and 78.1% at 1110 °C/0.1 s^{-1}, 1140 °C/0.1 s^{-1}, 1110 °C/0.01 s^{-1}, and 1110 °C/1 s^{-1}, respectively. These predicted values well agree with the test ones.

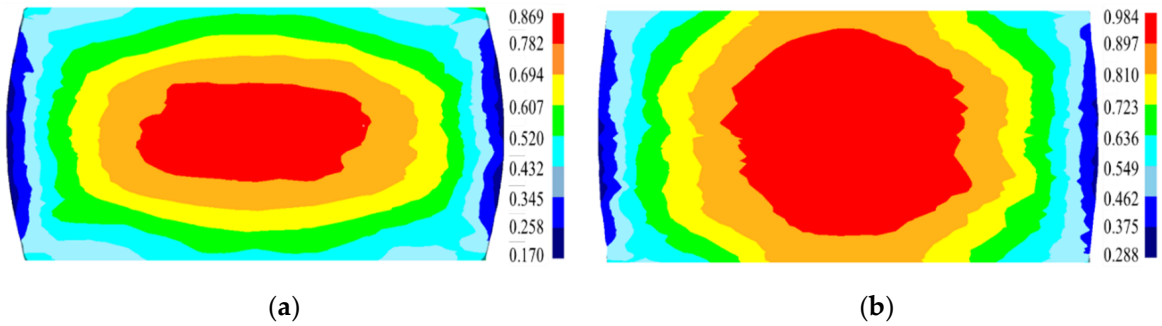

Figure 22. *Cont.*

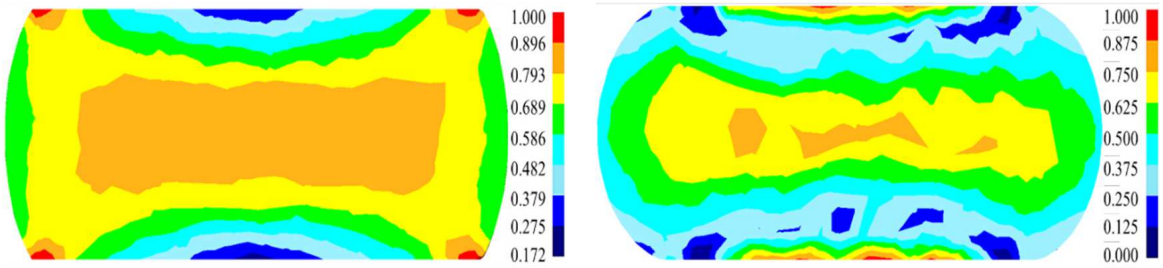

(**c**) (**d**)

Figure 22. The distribution of the simulated X_{drx} at (**a**) 1110 °C/0.1 s^{-1}; (**b**) 1140 °C/0.1 s^{-1}; (**c**) 1110 °C/0.01 s^{-1}; and (**d**) 1110 °C/1 s^{-1}.

Figure 23 exhibits the distribution of the simulated grain size under different deformation conditions. Obviously, the distribution of grain dimension is non-uniform at disparate deformation parameters. The average grain dimension in the large deformation zone gradually decreases when the strain rate is raised or the temperature is reduced. The experimental average grain sizes in the large deformation zone are 4.21 μm, 7.83 μm, 6.24 μm, and 2.27 μm, respectively, at 1110 °C/0.1 s^{-1}, 1140 °C/0.1 s^{-1}, 1110 °C/0.01 s^{-1}, and 1110 °C/1 s^{-1}, which coincide with the simulated results. The simulated X_{drx} and grain sizes in various deformation regions at 1110 °C/0.1 s^{-1} are quantitatively analyzed and are displayed in Figure 24 and Table 3. In Figure 24a, the DRX degree in the large deformation area is high while the average grain dimension is small. Also, the volume fraction of DRX in the non-central position is limited (the points P_2 and P_3 in Figure 24a), which is identical to the results from EBSD observation. Figure 24c,d) shows the variations of the simulated X_{drx} and average grain size at different positions with deformation time. The comparisons of the experimental/simulated X_{drx} and average grain size at 1110 °C/0.1 s^{-1} are shown in Table 3. It can be found that the simulation results well agree with the experimental ones. Thus, the results further indicate that the microstructure evolution can be accurately predicted by the proposed piecewise DRX kinetics equations and grain-growth model.

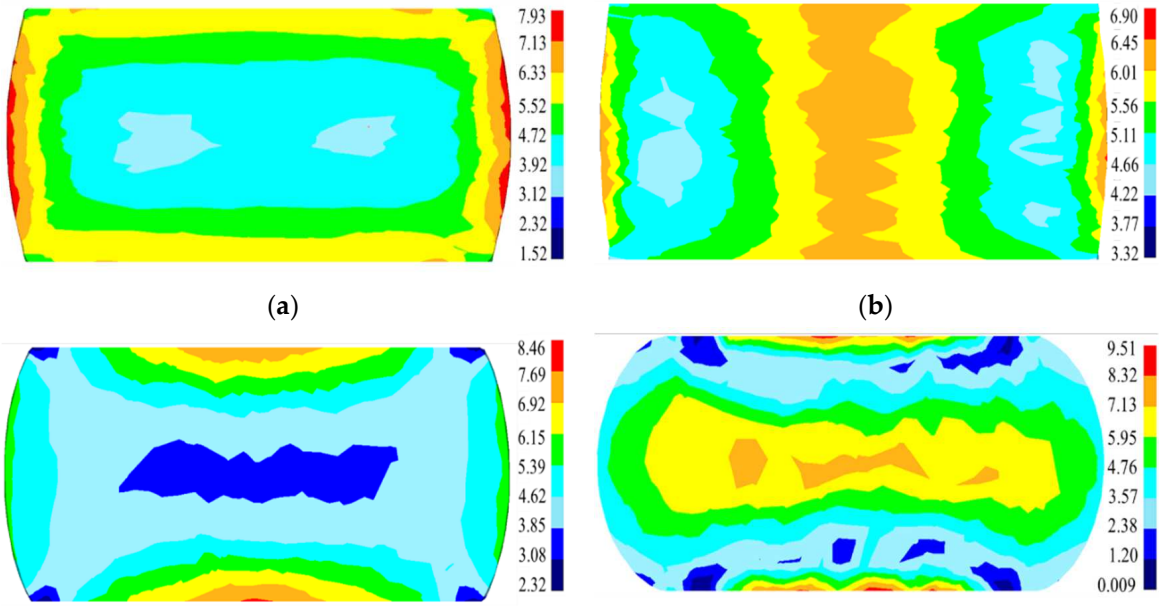

(**a**) (**b**)

(**c**) (**d**)

Figure 23. The distribution of the simulated grain size at (**a**) 1110 °C/0.1 s^{-1}; (**b**) 1140 °C/0.1 s^{-1}; (**c**) 1110 °C/0.01 s^{-1}; and (**d**) 1110 °C/1 s^{-1}.

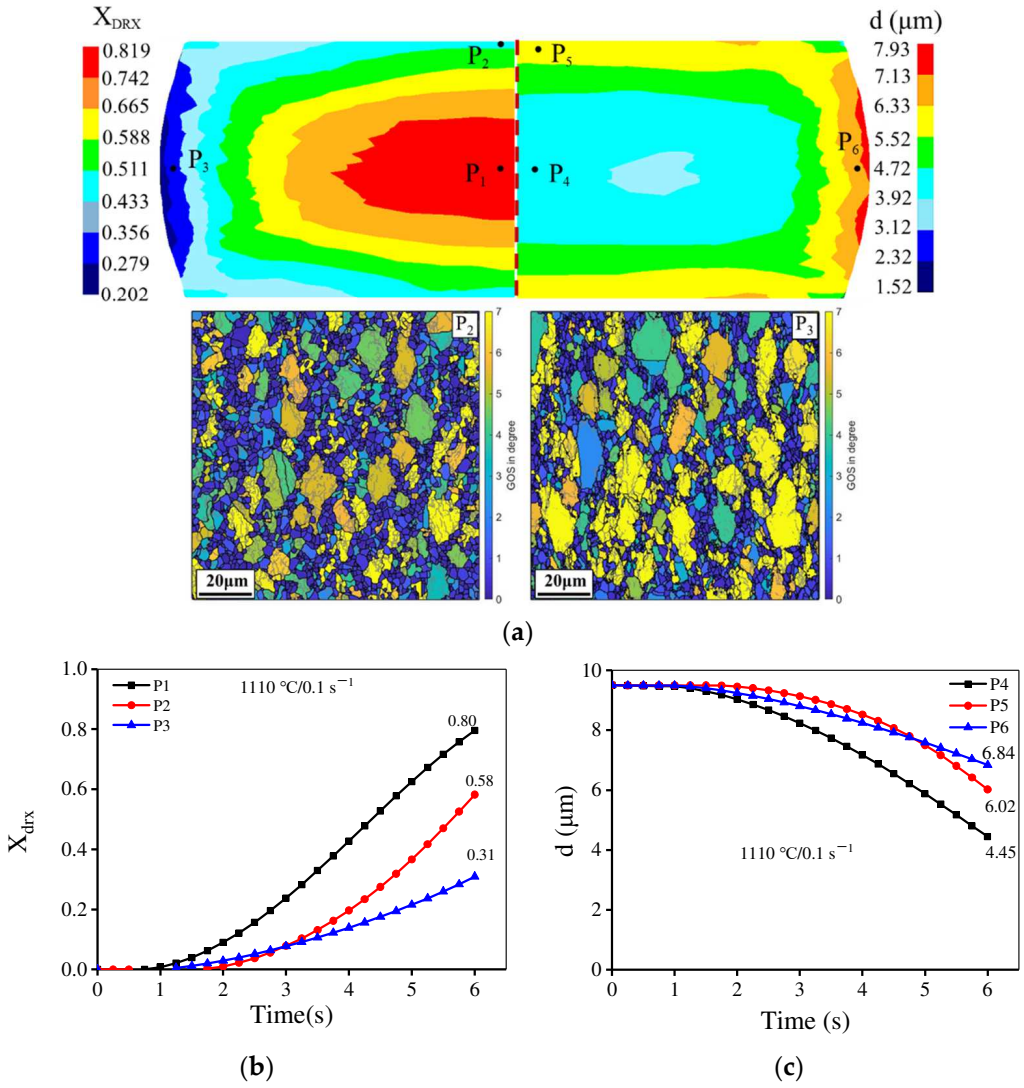

Figure 24. The simulated X_{drx} and average grain size in key points at 1110 °C/0.1 s^{-1} (**a**) Distribution of the simulated X_{drx} and average grain size; (**b**) The variation of the simulated X_{drx} with deformation time; (**c**) The variation of the simulated average grain size with deformation time.

Table 3. The comparisons of the experimental/simulated X_{drx} and average grain size at 1110 °C/0.1 s^{-1}.

Tracked Points	DRX Fraction (%)		Tracked Points	Average Grain Size (μm)	
	Experiment	Simulation		Experiment	Simulation
P_1	77.4	80	P_4	4.21	4.45
P_2	52.8	58	P_5	5.19	6.02
P_3	40.8	31	P_6	6.44	6.84

4. Conclusions

The DRX features and grain-growth behavior for a novel P/M superalloy are systematically studied. The piecewise DRX kinetics equations and grain-growth model are developed. The important conclusions are summarized:

1. The DRX behavior and grain features are sensitive to deformation parameters. The raised temperature/true strain can increase the volume fraction of DRX and the mean dimension of DRX grains. As the temperature is reduced or the true strain is raised, the mean grain dimension declines. Increasing the strain rate reduces the DRX volume fraction

and mean grain size. Moreover, the main DRX mechanism of the novel P/M superalloy is DDRX.

2. Piecewise DRX kinetics equations are proposed to predict DRX behavior in forming processes. The correlation coefficient of them is 0.992 and the average absolute relative error is 2.3%. Also, an accurate model is established to describe the grain-growth behavior during hot deformation.

3. The piecewise DRX kinetics equations and the grain growth equation are embedded into the DEFORM software using a secondary development method and the DRX features and grain-growth behavior in hot-compression processes are simulated. The simulated results show that the proposed piecewise DRX kinetics equations and grain-growth model can accurately depict the microstructure evolution of this novel P/M superalloy during hot deformation.

Author Contributions: Q.-M.Y.: Data curation, Investigation, Writing—original draft. Y.-C.L.: Conceptualization, Methodology, Supervision, Writing—review and editing. M.-S.C.: Data curation, Investigation. Z.-J.C.: Data curation, Investigation. All authors have read and agreed to the published version of the manuscript.

Funding: This work was supported by the National Natural Science Foundation of China (Grant No. 51975593), the Science and Technology Talent Promotion Project of Hunan Province (Grant No. 2020TJ-Q05), China, and the innovation project for graduate students of Central South University (Grant No. 1053320192150).

Institutional Review Board Statement: Not applicable.

Informed Consent Statement: Not applicable.

Data Availability Statement: The raw/processed data required to reproduce these findings cannot be shared at this time as the data also form part of an ongoing study.

Acknowledgments: This work was supported in part by the High Performance Computing Center of Central South University.

Conflicts of Interest: The authors declare no conflict of interest.

References

1. Wu, Y.T.; Li, C.; Xia, X.C.; Liang, H.Y.; Qi, Q.Q.; Liu, Y.C. Precipitate coarsening and its effects on the hot deformation behavior of the recently developed γ′-strengthened superalloys. *J. Mater. Sci. Technol.* **2021**, *67*, 95–104. [CrossRef]
2. Kumar, S.S.S.; Raghu, T.; Bhattacharjee, P.P.; Rao, G.A.; Borah, U. Work hardening characteristics and microstructural evolution during hot deformation of a nickel superalloy at moderate strain rates. *J. Alloys Compd.* **2017**, *709*, 394–409. [CrossRef]
3. Wu, H.X.; Ge, C.C.; Yan, Q.Z.; Xia, M.; Tian, T.; Zhu, Z.L.; Hu, Q.P. Plastic deformation behavior of spray formed superalloy FGH100. *Mater. Sci. Eng. A* **2017**, *699*, 156–164. [CrossRef]
4. Su, G.; Yun, Z.; Lin, Y.-C.; He, D.-G.; Zhang, S.; Chen, Z.-J. Microstructure evolution and a unified constitutive model of Ti-55511 alloy compressed at stepped strain rates. *Materials* **2021**, *14*, 6750. [CrossRef] [PubMed]
5. Lin, Y.-C.; He, D.-G.; Chen, M.-S.; Chen, X.-M.; Zhao, C.-Y.; Ma, X.; Long, Z.-L. EBSD analysis of evolution of dynamic recrystallization grains and δ phase in a nickel-based superalloy during hot compressive deformation. *Mater. Des.* **2016**, *97*, 13–24. [CrossRef]
6. Páramo-Kañetas, P.; Özturk, U.; Calvo, J.; Cabrera, J.M.; Guerrero-Mata, M. High-temperature deformation of delta-processed Inconel 718. *J. Mater. Process. Technol.* **2018**, *255*, 204–211. [CrossRef]
7. Lin, Y.-C.; Chen, X.-M. A critical review of experimental results and constitutive descriptions for metals and alloys in hot working. *Mater. Des.* **2011**, *32*, 1733–1759. [CrossRef]
8. Kumar, S.S.S.; Raghu, T.; Bhattacharjee, P.P.; Appa Rao, G.; Borah, U. Evolution of microstructure and microtexture during hot deformation in an advanced P/M nickel base superalloy. *Mater. Charact.* **2018**, *146*, 217–236. [CrossRef]
9. Tan, L.M.; Li, Y.P.; He, G.A.; Liu, F.; Nie, Y.; Jiang, L. Optimized hot workability of a powder metallurgy nickel-base superalloy. *Mater. Charact.* **2019**, *147*, 340–352. [CrossRef]
10. Liu, G.W.; Mao, C.L.; Ding, R.; Yu, L.M.; Liu, C.X.; Liu, Y.C. The kinetics of dynamic recrystallization and construction of constitutive modeling of RAFM steel in the hot deformation process. *J. Nucl. Mater.* **2021**, *557*, 153285. [CrossRef]
11. Azarbarmas, M.; Aghaie-Khafri, M.; Cabrera, J.M.; Calvo, J. Dynamic recrystallization mechanisms and twining evolution during hot deformation of Inconel 718. *Mater. Sci. Eng. A* **2016**, *678*, 137–152. [CrossRef]
12. Fang, B.; Tian, G.F.; Ji, Z.; Wang, M.Y.; Jia, C.C.; Yang, S.W. Study on the thermal deformation behavior and microstructure of FGH96 heat extrusion alloy during two-pass hot deformation. *Int. J. Min. Metall. Mater.* **2019**, *26*, 657–663. [CrossRef]

13. Zhang, C.; Zhang, L.W.; Li, M.F.; Shen, W.F.; Gu, S.D. Effects of microstructure and γ′ distribution on the hot deformation behavior for a powder metallurgy superalloy FGH96. *J. Mater. Res.* **2014**, *29*, 2799–2808. [CrossRef]
14. Wang, S.Y.; Fang, S.; Shi, Z.S.; Jiang, J.Y.; Zhou, X.M.; Lin, J.G. Direct powder forging of PM nickel-based superalloy: Densification and recrystallisation. *Int. J. Adv. Manuf. Technol.* **2017**, *88*, 2661–2670. [CrossRef]
15. Zhang, M.J.; Li, F.G.; Wang, L.; Wang, S.Y. Investigations of inhomogeneous mechanical properties and plastic deformations in HIPed P/M nickel-base superalloy FGH96 by using micro-indentation methods. *Mater. Sci. Eng. A* **2012**, *556*, 233–245. [CrossRef]
16. Sreenu, B.; Sarkar, R.; Kumar, S.S.S.; Chatterjee, S.; AppaRao, G. Microstructure and mechanical behaviour of an advanced powder metallurgy nickel base superalloy processed through hot isostatic pressing route for aerospace applications. *Mater. Sci. Eng. A* **2020**, *797*, 140254. [CrossRef]
17. Sohrabi, M.J.; Mirzadeh, H. Estimation of homogenisation time for superalloys based on a new diffusional model. *Mater. Sci. Technol.* **2020**, *36*, 380–384. [CrossRef]
18. Jiang, Y.Q.; Lin, Y.-C.; Wang, G.Q.; Pang, G.D.; Chen, M.S.; Huang, Z.C. Microstructure evolution and a unified constitutive model for a Ti-55511 alloy deformed in β region. *J. Alloys Compd.* **2021**, *870*, 159534. [CrossRef]
19. Ahmadi, H.; Ashtiani, H.R.R.; Heidari, M. A comparative study of phenomenological, physically-based and artificial neural network models to predict the Hot flow behavior of API 5CT-L80 steel. *Mater. Today Commun.* **2020**, *25*, 101528. [CrossRef]
20. He, D.-G.; Lin, Y.-C.; Chen, M.-S.; Li, L. Kinetics equations and microstructural evolution during metadynamic recrystallization in a nickel-based superalloy with δ phase. *J. Alloys Compd.* **2017**, *690*, 971–978. [CrossRef]
21. Bobbili, R.; Ramudu, B.V.; Madhu, V. A physically-based constitutive model for hot deformation of Ti-10-2-3 alloy. *J. Alloys Compd.* **2017**, *696*, 295–303. [CrossRef]
22. Badrish, A.; Morchhale, A.; Kotkunde, N.; Singh, S.K. Influence of material modeling on warm forming behavior of nickel based super alloy. *Int. J. Mater. Form.* **2020**, *13*, 445–465. [CrossRef]
23. Rezaei Ashtiani, R.; Shahsavari, P. Constitutive modeling of flow behavior of precipitation-hardened AA7022-T6 aluminum alloy at elevated temperature. *Trans. Nonferrous Met. Soc. China* **2020**, *30*, 2927–2940. [CrossRef]
24. Liu, Y.H.; Ning, Y.Q.; Yang, X.M.; Yao, Z.K.; Guo, H.Z. Effect of temperature and strain rate on the workability of FGH4096 superalloy in hot deformation. *Mater. Des.* **2016**, *95*, 669–676. [CrossRef]
25. Liu, Y.H.; Yao, Z.K.; Ning, Y.Q.; Nan, Y. Effect of deformation temperature and strain rate on dynamic recrystallized grain size of a powder metallurgical nickel-based superalloy. *J. Alloys Compd.* **2017**, *691*, 554–563. [CrossRef]
26. Zhang, M.; Liu, G.Q.; Wang, H.; Hu, B.F. Modeling of thermal deformation behavior near γ′ solvus in a Ni-based powder metallurgy superalloy. *Comp. Mater. Sci.* **2019**, *156*, 241–245. [CrossRef]
27. Tan, G.; Li, H.-Z.; Wang, Y.; Qiao, S.-C.; Yang, L.; Huang, Z.-Q.; Cheng, T.-W.; Zhao, Z.-X. Effect of Zener-Hollomon parameter on microstructure evolution of a HEXed PM nickel-based superalloy. *J. Alloys Compd.* **2021**, *874*, 159889. [CrossRef]
28. Yang, Q.-M.; Lin, Y.-C.; Guo, J.-Z.; Wang, C.; Chen, Z.-J.; Chen, K.-G.; Zhu, J.-C. Spheroidization and dynamic recrystallization mechanisms of a novel HIPed P/M superalloy during hot deformation. *J. Alloys Compd.* **2022**, *910*, 16490. [CrossRef]
29. Badrish, C.A.; Kotkunde, N.; Mahalle, G.; Singh, S.K.; Mahesh, K. Analysis of hot anisotropic tensile flow stress and strain hardening behavior for Inconel 625 alloy. *J. Mater. Eng. Perform.* **2019**, *28*, 7537–7553. [CrossRef]
30. Wen, D.-X.; Lin, Y.-C.; Chen, J.; Chen, X.-M.; Zhang, J.-L.; Liang, Y.-J.; Li, L.-T. Work hardening behaviors of typical solution-treated and aged Ni-based superalloys during hot deformation. *J. Alloys Compd.* **2015**, *618*, 372–379. [CrossRef]
31. Lin, Y.-C.; Wen, D.-X.; Chen, M.-S.; Chen, X.-M. A novel unified dislocation density-based model for hot deformation behavior of a nickel-based superalloy under dynamic recrystallization conditions. *Appl. Phys. A* **2016**, *122*, 805. [CrossRef]
32. Chen, Z.-J.; Lin, Y.-C.; He, D.-G.; Lou, Y.-M.; Chen, M.-S. A unified dislocation density-based model for an aged polycrystalline Ni-based superalloy considering the coupled effects of complicate deformation mechanisms and initial δ phase. *Mater. Sci. Eng. A* **2021**, *827*, 142062. [CrossRef]
33. Momeni, A.; Abbasi, S.M.; Morakabati, M.; Badri, H. A comparative study on the hot working behavior of Inconel 718 and ALLVAC 718 plus. *Metall. Mater. Trans. A* **2017**, *48*, 1216–1229. [CrossRef]
34. Xie, B.; Zhang, B.; Ning, Y.; Fu, M.W. Mechanisms of DRX nucleation with grain boundary bulging and subgrain rotation during the hot working of nickel-based superalloys with columnar grains. *J. Alloys Compd.* **2019**, *786*, 636–647. [CrossRef]
35. Jia, D.; Sun, W.; Xu, D.; Yu, L.; Xin, X.; Zhang, W.; Qi, F. Abnormal dynamic recrystallization behavior of a nickel based superalloy during hot deformation. *J. Alloys Compd.* **2019**, *787*, 196–205. [CrossRef]
36. Yin, X.-Q.; Park, C.-H.; Li, Y.-F.; Ye, W.-J.; Zuo, Y.-T.; Lee, S.-W.; Yeom, J.-T.; Mi, X.-J. Mechanism of continuous dynamic recrystallization in a 50Ti-47Ni-3Fe shape memory alloy during hot compressive deformation. *J. Alloys Compd.* **2017**, *693*, 426–431. [CrossRef]
37. Zhang, H.B.; Zhang, K.F.; Zhou, H.P.; Lu, Z.; Zhao, C.H.; Yang, X.L. Effect of strain rate on microstructure evolution of a nickel-based superalloy during hot deformation. *Mater. Des.* **2015**, *80*, 51–62. [CrossRef]
38. Hadadzadeh, A.; Mokdad, F.; Wells, M.A.; Chen, D.L. A new grain orientation spread approach to analyze the dynamic recrystallization behavior of a cast-homogenized Mg-Zn-Zr alloy using electron backscattered diffraction. *Mater. Sci. Eng. A* **2018**, *709*, 285–289. [CrossRef]
39. Alvi, M.H.; Cheong, S.W.; Weiland, H.; Rollett, A.D. Recrystallization and texture development in hot rolled 1050 aluminum. *Mater. Sci. Forum Trans. Tech. Publ.* **2004**, *467–470*, 357–362.

40. Lin, Y.-C.; Wu, X.-Y.; Chen, X.-M.; Chen, J.; Wen, D.-X.; Zhang, J.-L.; Li, L.-T. EBSD study of a hot deformed nickel-based superalloy. *J. Alloys Compd.* **2015**, *640*, 101–113.
41. Annasamy, M.; Haghdadi, N.; Taylor, A.; Hodgson, P.; Fabijanic, D. Dynamic recrystallization behaviour of AlxCoCrFeNi high entropy alloys during high-temperature plane strain compression. *Mater. Sci. Eng. A* **2019**, *745*, 90–106. [CrossRef]
42. Momeni, A.; Abbasi, S.M.; Morakabati, M.; Badri, H.; Wang, X. Dynamic recrystallization behavior and constitutive analysis of Incoloy 901 under hot working condition. *Mater. Sci. Eng. A* **2014**, *615*, 51–60. [CrossRef]
43. Mirzadeh, H.; Roostaei, M.; Parsa, M.H.; Mahmudi, R. Rate controlling mechanisms during hot deformation of Mg–3Gd–1Zn magnesium alloy: Dislocation glide and climb, dynamic recrystallization, and mechanical twinning. *Mater. Des.* **2015**, *68*, 228–231. [CrossRef]
44. Xia, Y.-C.; Chen, X.-M.; Lin, Y.-C.; Lu, X.-Z. Evolution of annealing twins in a hot deformed nickel-based superalloy. *Materials* **2022**, *15*, 7. [CrossRef]
45. Jiang, H.; Dong, J.X.; Zhang, M.C.; Yao, Z.H. A study on the effect of strain rate on the dynamic recrystallization mechanism of alloy 617B. *Metall. Mater. Trans. A* **2016**, *47*, 5071–5087. [CrossRef]
46. Charpagne, M.A.; Franchet, J.M.; Bozzolo, N. Overgrown grains appearing during sub-solvus heat treatment in a polycrystalline γ-γ′ Nickel-based superalloy. *Mater. Des.* **2018**, *144*, 353–360. [CrossRef]
47. Wang, G.-Q.; Chen, M.-S.; Li, H.-B.; Lin, Y.-C.; Zeng, W.-D.; Ma, Y.-Y. Methods and mechanisms for uniformly refining deformed mixed and coarse grains inside a solution-treated Ni-based superalloy by two-stage heat treatment. *J. Mater. Sci. Technol.* **2021**, *77*, 47–57. [CrossRef]
48. Poliak, E.I.; Jonas, J.J. A one-parameter approach to determining the critical conditions for the initiation of dynamic recrystallization. *Acta Mater.* **1996**, *44*, 127–136. [CrossRef]
49. Chen, M.-S.; Lin, Y.-C.; Li, K.-K.; Zhou, Y. A new method to establish dynamic recrystallization kinetics model of a typical solution-treated Ni-based superalloy. *Comput. Mater. Sci.* **2016**, *122*, 150–158. [CrossRef]
50. Huang, H.L.; Liu, G.Q.; Wang, H.; Ullah, A.; Hu, B.F. Dissolution behavior and kinetics of γ′ phase during solution treatment in powder metallurgy nickel-based superalloy. *Metall. Mater. Trans. A* **2020**, *51*, 1075–1084. [CrossRef]
51. Lin, Y.-C.; Wen, D.-X.; Chen, M.-S.; Liu, Y.-X.; Chen, X.-M.; Ma, X. Improved dislocation density based models for describing hot deformation behaviors of a Ni-based superalloy. *J. Mater. Res.* **2016**, *31*, 2415–2429. [CrossRef]